



Synchrotron X-ray micro-computed tomography imaging of 3D re-entrant micro lattice during in situ micro compression experimental process

Wenwang Wu^{a,*}, Dexion Qi^b, Wenxia Hu^b, Li Xi^{b,*}, Lijuan Sun^c, Binbin Liao^b, Filippo Berto^d, Guian Qian^c, Dengbao Xiao^{b,*}

^a Department of Engineering Mechanics, School of Naval Architecture, Ocean and Civil Engineering, Shanghai Jiao Tong University, Shanghai, 200240, China

^b Institute of Advanced Structure Technology, Beijing Institute of Technology, Beijing, 100081, PR China

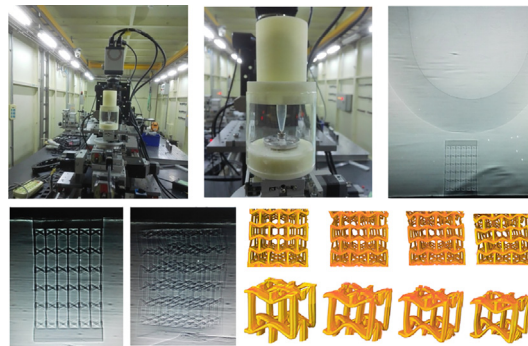
^c State Key Laboratory of Nonlinear Mechanics (LNM), Institute of Mechanics, Chinese Academy of Sciences, Beijing 100190, China

^d Department of Mechanical and Industrial Engineering, Norwegian University of Science and Technology (NTNU), Richard Birkelandsvei 2b, 7491 Trondheim, Norway

HIGHLIGHTS

- In situ compression X-Ray tomography tests (PμLSE) for 3D micro re-entrant lattice reveal process-induced internal defects.
- PμLSE process induced internal defects are characterized for 3D micro re-entrant lattice.
- The influence of defects on mechanical properties of 3D micro re-entrant lattice is revealed.

GRAPHICAL ABSTRACT



ARTICLE INFO

Article history:

Received 8 October 2019

Received in revised form 19 April 2020

Accepted 20 April 2020

Available online 22 April 2020

Keywords:

3D re-entrant

Synchrotron X-ray tomography

Mechanical properties

Projection Micro Litho Stereo Exposure (PμLSE)

ABSTRACT

3D re-entrant mechanical metamaterials were designed and fabricated with PμLSE (Projection Micro Litho Stereo Exposure) 3D printing technique, synchrotron X-Ray tomography 3D imaging and in situ mechanical experiments were performed for characterizing additive manufacturing (AM) process induced internal defects, corresponding relations between defects and mechanical behaviors of harvested 3D re-entrant lattice samples were explored through experiments and simulations comparisons. Firstly, in situ micro compression mechanical test device was designed and constructed for in situ synchrotron X-Ray 3D tomography mechanical experiments; Afterwards, interrupted in situ compression tests were performed for investigating the effects of manufacturing process induced defects on the deformation behaviors of 3D re-entrant lattice metamaterials, and finite element (FE) modeling was performed and compared with experimental results for understanding the mechanical behaviors of as-fabricated 3D re-entrant lattice metamaterials.

© 2020 The Authors. Published by Elsevier Ltd. This is an open access article under the CC BY-NC-ND license (<http://creativecommons.org/licenses/by-nc-nd/4.0/>).

* Corresponding authors.

E-mail addresses: wuwenwang2014@163.com (W. Wu), xili@bit.edu.cn (L. Xi), xdbhangtian@163.com (D. Xiao).

1. Introduction

In recent decades, auxetic materials and structures with negative Poisson's ratio (NPR) are proposed for various types of multifunctional applications, such as: impact energy absorption, vibration attenuation, negative and zero thermal expansion, heat flow management, etc. [1–12]. According to the structural deformation models, auxetic structures can be classified into following categories: missing-rib, rigid (or semi-rigid) rotation, re-entrant, chiral and elastic instability, etc. [13–19]. Evolutionary algorithm was proposed for designing re-entrant auxetic with tunable Poisson's ratio distribution, and comparisons between experiments and finite element simulations were performed for verification [20]. Theoretical formulas were derived for predicting the NPR deformation behaviors of re-entrant and anti-trichiral hybrid honeycombs under large deformation, corresponding deformation mechanisms and stress-strain curves were investigated through experimental and numerical simulation comparisons [21]. Based on Castiglione's second theorem, analytical model with five geometrical parameters was developed for studying the mechanical properties of star-shaped re-entrant auxetic structures, where corresponding stretching, transverse shearing and bending deformations were explored [22]. The deformation mode, crushing stress and Poisson's ratio distribution of graded auxetic re-entrant honeycomb were studied through experiments and finite element comparisons [23]. Damage characterizations and mechanical behaviors of 3D re-entrant lattices fabricated with selective laser melting (SLM) 3D printing technique were investigated with in situ interrupted micro-CT tests, numerical simulations were performed for studying the effects of defects on the mechanical performances and underlying failure mechanisms of 3D re-entrant lattices [24]. A strain-based expansion homogenization method was proposed for analyzing the elastic mechanical behaviors of auxetic cellular structure [25], which can be used as guidance for function-oriented design of re-entrant auxetic cellular structures. The in-plane shear modulus of re-entrant hexagonal honeycombs under large deformation was investigated through theoretical analysis and numerical simulation comparisons [26]. The energy absorption performances of novel auxetic re-entrant star-shaped honeycombs were investigated through theory analysis and finite element modeling, and three types of deformation modes were detected under different impact velocities [27]. Based on energy methods, the mechanical behaviors of 3D auxetic lattice structures were investigated through theoretical analysis and experimental comparisons, and influence of strut slenderness variation on the deformation mechanisms of the structure was also discussed [28].

In recent decades, various types of 3D additive manufacturing (AM) techniques are developed for manufacturing lattice structures. However, manufacturing defects induced surface roughness, internal voids and cracks will reduce the mechanical integrity and physical performances of fabricated lattice structures, it is important to quantitatively assess the manufacturing defects and analyze the relation between defects and mechanical performances of fabricated lattice structures [29–33]. Finite element models based on micro-computer tomography (μ CT) analysis and representation of elliptical strut cross-sections of SLM fabricated struts were proposed for qualifying the mechanical integrity of lattice structures [34]. X-ray tomography 3D imaging was combined with finite element computations for predicting the mechanical properties of cellular structures manufactured with stereolithography 3D printing technique, where randomly distributed spherical voids were identified [35]. In situ X-ray tomography 3D imaging of additive manufactured hollow 3D lattice structures under compression loading was performed, and 3D image-based conformal finite element model was performed and compared with experiments using Gurson-Tvergaard-Needleman (GTN) porous plasticity [36]. Liu et al. [37] performed interrupted quasi-static compression tests of selected laser sintering (SLS) additive manufactured metallic lattices with regular octet and rhombicuboctahedron unit cells, and statistical physical

models of defects distributions were constructed. In situ synchrotron X-Ray micro-tomography uniaxial compression tests were performed for two types of 3D lattice structures, demonstrating that manufacturing defects were responsible for the heterogeneous localized deformation [38]. The shearing mechanical performances of single-layer tetrahedral trusses fabricated by rapid prototyping and investment casting were studied through experimental, theoretical and simulation comparisons, it was found that casting defects can contribute significantly to experimental results deviation [39]. Sercombe et al. [40] studied the failure process of topology-optimized structures via interrupted compression testing and X-ray micro-tomography characterization.

In this paper, in situ micro compression device used for investigating the deformation process and failure mechanisms of advanced materials and structures under synchrotron X-Ray 3D imaging conditions is designed and fabricated. Fabrications of 3D re-entrant mechanical metamaterials samples with high temperature resistance photosensitive resin HTL® developed by BMF® Material Technology Inc. are performed with PµLSE (Projection Micro Litho Stereo Exposure) 3D printing technology. Finally, interrupted in situ compression tests are performed for investigating the effects of manufacturing process induced defects on the deformation behaviors of 3D re-entrant lattice metamaterials, finite element (FE) modeling is performed for comparison with experimental results, and quantitative characterizations of defects are performed for understanding the mechanical behaviors of as-fabricated 3D re-entrant lattice metamaterials.

2. Sample fabrication and interrupted in situ compression experiments

2.1. Mechanical design and fabrication of 3D re-entrant lattice structures

As shown in Fig. 1(a)–(b), the geometrical parameters of 3D re-entrant unit cell are: t , l and h , which are corresponding to the side length of strut cross section, length of oblique strut and length of vertical strut, respectively. θ is the angle between oblique strut and vertical strut. As shown in Fig. 1(c), global geometrical parameters of 3D re-entrant compression sample along x , y and z directions are: L_x , L_y and L_z respectively. The relative density of the designed re-entrant lattice unit cell is written as [28]:

$$\bar{\rho} = \frac{t^2(H + 4L)}{2l^2 \sin^2\theta(h - l \cos\theta)}, \quad (1)$$

where $H = h + \frac{t(1 - \cos\theta)}{\sin\theta}$, $L = (l - \frac{t}{\sin\theta})$, t , l and h are the side length of the strut cross section, the length of the oblique re-entrant strut and the length of the vertical strut, respectively. θ is the angle between the oblique strut and the vertical strut. Poisson's ratio and the effective modulus along Z direction under compressive stress can be written as [24]:

$$\nu_{zx} = \frac{-5 \cos\theta (GL^2 + 6Et)(\alpha - \cos\theta)}{(L^2 + 6t^2) \sin^2\theta + 4\alpha t^2}, \quad (2)$$

$$E_z = \frac{\frac{t^2(h - l \cos\theta)}{l^2 \sin^2\theta}}{(l - 2\Delta l) \sin^2\theta \left(\frac{(l - 2\Delta l)^2}{2E_s t^2} + \frac{3}{5G_s} \right) + \frac{(l - 2\Delta l) \cos^2\theta + 2(h - 2\Delta h)}{2E_s}}, \quad (3)$$

where, E is the modulus of constituent materials.

Geometrical details of the designed 3D re-entrant lattice are shown in Table 1.

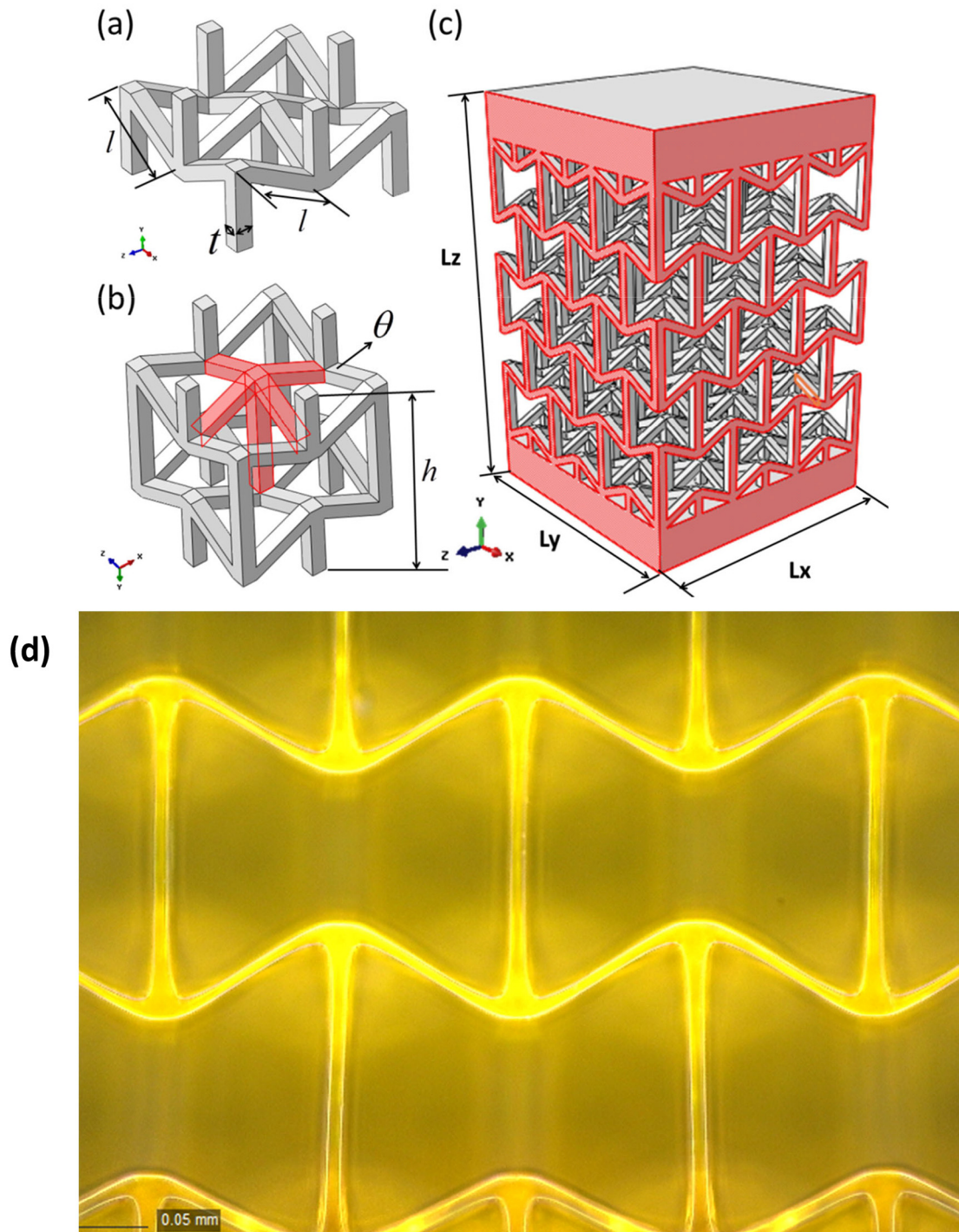


Fig. 1. Microstructure design of 3D re-entrant lattice mechanical metamaterials for compression tests, and microstructure of as-fabricated 3D re-entrant lattice sample under optical microscopy: (a), half unit cell; (b), unit cell; (c), designed sample; (d), optical image of as-fabricated sample.

As shown in Fig. 2, PμLSE 3D printing technique is a lithography-based additive manufacturing technique. Firstly, a 3D model is generated using computer-aided-design (CAD) software, and digitally sliced into a series of cross-sectional images of the 3D model. Each digital sliced image is transferred through digital mask pattern illuminated

with ultra-violet (UV) light source, which is then projected through a reduction lens and focused on the surface of photo-curable resin. Afterwards, the patterned UV light converts liquid resin to a solid layer through photo-polymerization, where the UV light energy, intensity, illumination duration can be optimized. Once a layer is formed, the

Table 1
Geometrical parameters of the as-fabricated 3D re-entrant sample.

Unit cell				Sample geometry		
$h = 350\mu\text{m}$	$l = 250\mu\text{m}$	$t = 25\mu\text{m}$	$\theta = 63.45^\circ$	$Lx = 0.775 \text{ mm}$	$Ly = 0.775 \text{ mm}$	$Lz = 1.21 \text{ mm}$

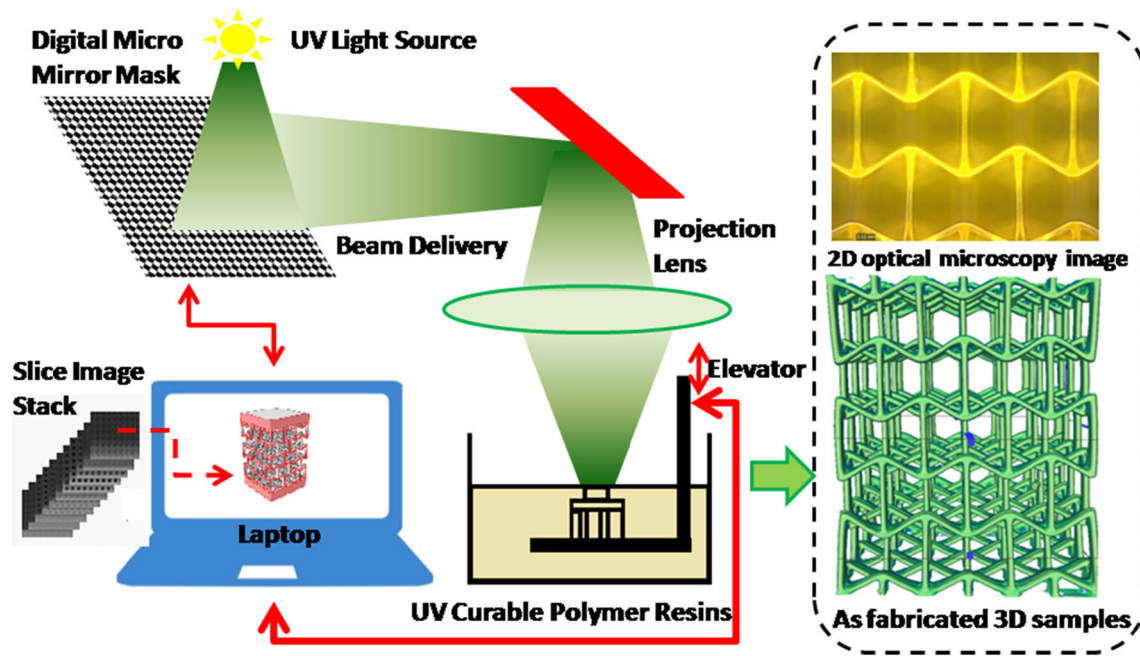


Fig. 2. The manufacturing process of Projection Micro Litho Stereo Exposure 3D printing technique.

transit elevator will deliver the sample holder downwards, thus introducing fresh liquid resin for further photo-polymerization of the next layer, such process is repeated until all the layers are complete for harvesting the expected 3D samples with complex microstructures. The μ LSE 3D printing technique can be employed for the fabrication of lightweight metastructures with extraordinary stiffness and strength for lightweight applications in aerospace engineering, lightweight energy absorption materials and structures for automobile industries, mechanical metamaterials for sound absorption and vibration attenuation, etc.

In the following, high precision projection micro-stereolithography technique was employed for 3D re-entrant sample fabrication, and all the samples were fabricated with nanoArch® S130 3D printing machine, (constructed by BMF® Precision Technology Co, Ltd., Shenzhen, China). The materials employed for printing were high temperature resistance photosensitive resin HTL® (the main compositions of HTL® are acrylic resin) developed by BMF® Material Technology Inc. The 3D printing fabrication spatial resolution was $2\text{ }\mu\text{m}$, and a 405 nm light-emitting diode (LED) UV light source was employed for generating light intensity of 45 mW/cm^2 , and the exposure time was 1 s during the printing process. After 3D printing from the resin pool, the harvested raw lattice sample was cleaned with isopropyl alcohol (IPA) for 30 s to dissolve the residual liquid resin off the lattice sample. Then, the lattice was dried in an oven at $50\text{ }^\circ\text{C}$ for 10 min, and illuminated with UV light at 35 mW/cm^2 intensity for final solidification of lattice sample. Totally, 5 pieces of 3D re-entrant lattice structures were harvested for the following in situ compression experiments and defects characterization.

2.2. In situ compression device under synchrotron X-ray tomography condition

As shown in Fig. 3, cylindrical tube with axial displacement generator and micro-force measurement components was designed for in situ micro-compression experiments. The axial displacement was generated through piezoelectric ceramic cylindrical tube manufactured by Daheng Optoelectronics Co. Ltd., where the axial translational resolution was $0.8\text{ }\mu\text{m/V}$, and the voltage range of piezoelectric ceramic cylindrical tube was: 0–220 V. Plastic tube indenter with tiny elliptical cone was attached to the bottom of piezoelectric ceramic cylindrical tube, which

can transfer compression loading onto 3D re-entrant sample. The strain-gauge based disk-shape miniature load cell (manufactured by Shanghai ForceChina Measurement Technology Co, Ltd.) was employed and amounted at the bottom for measuring the compression force during in situ compression process, the 3D re-entrant lattice sample was amounted on the top of the disk-shape load cell, and the force output maximum was 10.0 N, with micro-force measurement resolution $50\text{ }\mu\text{N}$. In situ compression test, synchrotron X-Ray tomography 3D imaging and 3D image reconstruction techniques were employed for acquiring the 3D internal deformation features and failure process of as-fabricated 3D re-entrant lattice metamaterials during interrupted in situ compression experiments.

2.3. Mechanical properties of additive manufacturing materials

Tensile experiments were performed for testing the mechanical properties of high temperature resistance photosensitive resin HTL® developed by BMF® Material Technology Inc., which was used for manufacturing the 3D re-entrant micro lattice samples. Totally, 10 pieces of dog-bone shape tensile samples were prepared and tested, and uniaxial tensile tests were performed on Instron®5985 machine at constant strain rate of 10^{-4} s^{-1} , the harvested average elastic modulus and ultimate strain were shown in Table 2.

3. In situ compression experiment and synchrotron X-Ray tomography

High resolution synchrotron radiation micro computed tomography (SR- μ CT) experiments were performed at BL13W1 beam line station of Shanghai Synchrotron Radiation Facility, China. Fig. 3(a) and (b) were the tomography experimental devices and systems at BL13W1 beam line station, where the energy of X-Ray was in the range from 8 keV to 72.5 keV. The detector of this system was able to harvest tomography images with pixel resolution range from $0.32\text{ }\mu\text{m/pixel}$ to $24\text{ }\mu\text{m/pixel}$. Considering the trade-off between sample size and X-Ray beam field-of-view requirements, spatial resolution for reconstructed tomography image was set to $0.65\text{ }\mu\text{m/pixel}$ for the following experiments. During the experiments, the specimen was rotated 180° around the vertical axis with an angular increment 0.25° per rotation step. The detailed X-Ray tomography experimental conditions for 3D re-entrant lattice

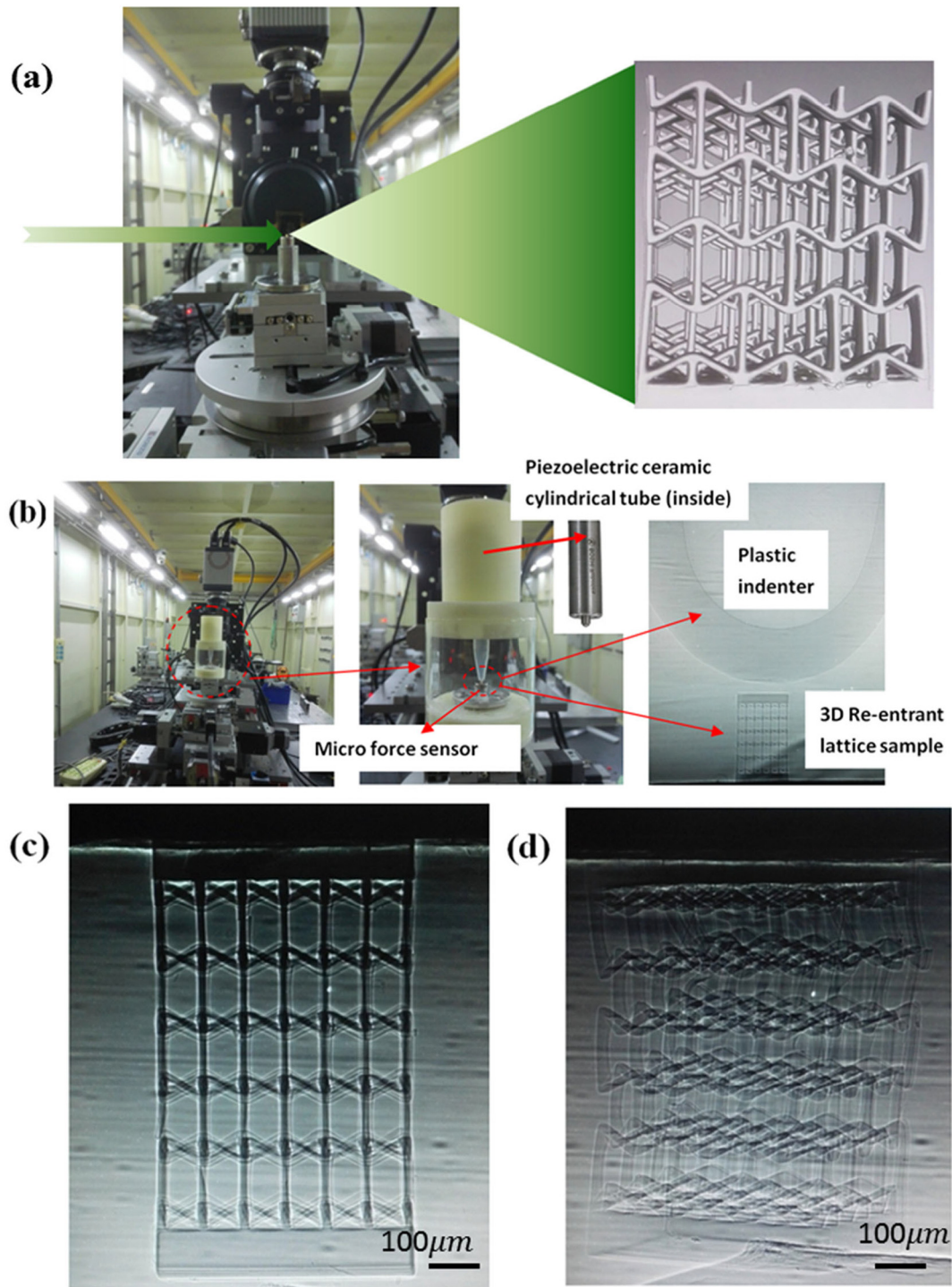


Fig. 3. Microstructure characterization of as-fabricated 3D re-entrant lattice samples, combining in situ interrupted compression test device and 3D X-ray micro-tomography imaging technique: (a), X-Ray tomography 3D imaging process; (b), in situ compression tomography system; (c), grey image projected onto the detector generated by X-Ray absorption before compression; (d) grey image projected on the detector generated by X-Ray absorption after compression at strain level $\varepsilon_z = 7.1\%$.

Table 2

Measured materials properties of the HTL® for 3D printing.

Materials	Modulus of elasticity	Poisson's ratio ^a	Ultimate strain
HTL®	$E = 742 \pm 2.5 \text{ MPa}$	0.35	0.20 ± 0.023

^a Note this value for Poisson's ratio was not measured directly; instead it was obtained from material suppliers.

samples were: X-ray beam energy of 18 keV, pixel size of $0.65 \mu\text{m}/\text{pixel}$, space of 0.1 m between sample and detector, and exposure time of 500 ms for each rotation angle increment step. After calibrating the micro force sensor of the in situ compression device, the 3D re-entrant lattice sample was amounted onto the top surface of the disk shape load cell, and the compression force during the in situ compression process was measured with the disk shape load cell. Micro axial translational displacement was generated through adjusting the voltage input of the piezoelectric ceramic cylindrical tube, then further transmitted onto the top of the 3D re-entrant lattice sample for generating

compressive deformation. Based on above displacement generation and compression force measurement schemes, interrupted in situ compression tests under X-ray tomography 3D imaging conditions were performed accordingly, where the 3D re-entrant sample was rotated around axial for 180° at 0.25° for each interrupted step, and 3D image stacks containing 3D internal deformation information of samples were harvested accordingly. Fig. 4(a) was the cross-section sliced images of harvested X-Ray tomography 3D images, within xz, yz and xy planes, respectively. It was found that the as-fabricated struts and joint nodes along y direction were thicker than along x and z directions. Similar to melting icicles with frozen droplets on the tips induced by gravity, the geometry of strut and joint node related to y direction was elongated due to self-weight gravity driven viscous fluid during P μ LSE additive manufacturing process. Statistical analysis was performed for characterizing the surface roughness and internal defects qualitatively, whereby the statistical geometrical parameters of struts along different directions and strut joints were analyzed. Consequently, several typical types of defects were identified: (a) holes at the joints of the strut and irregular side length deviations of the strut; (b) irregular bulges, grooves in the 3D re-entrant lattice structure. All of these defects were related to the building direction, due to self-weight induced distortion, and viscous fluid during the P μ LSE additive manufacturing process. As shown in Fig. 4(b) and (c), totally 3 interrupted compression loading

steps were applied, global deformation process and local deformation of unit cell in the middle of the 3D re-entrant samples were harvested, corresponding to strain level: $\varepsilon_z=4.4\%$, 7.1% and 11.5% , respectively.

4. Results analysis and discussion

As shown in Fig. 5, the strain-stress curve of interrupted in situ experiments was compared with finite element simulated results, experimental stress dropped as a result of interrupted tomography imaging, and the experimental recorded stress was higher than FEA simulated results, this is because of the additive manufacturing process induced defects, these defects are strut surface roughness, strut crosssection geometrical shape deviation from designed ideal geometries, which are formed due to self-weight induced viscous fluid during the cross-linking curing reaction process of photosensitive resin during the P μ LSE additive manufacturing process. These defects can be observed through synchrotron X-ray micro-computed tomography images, as shown in Fig. 4(a). The as-fabricated struts were remarkably elongated along the building direction during P μ LSE 3D printing process due to gravity induced viscous fluid during solidification process, and the bending stiffness of struts related to the direction perpendicular to the building direction was remarkably enhanced.

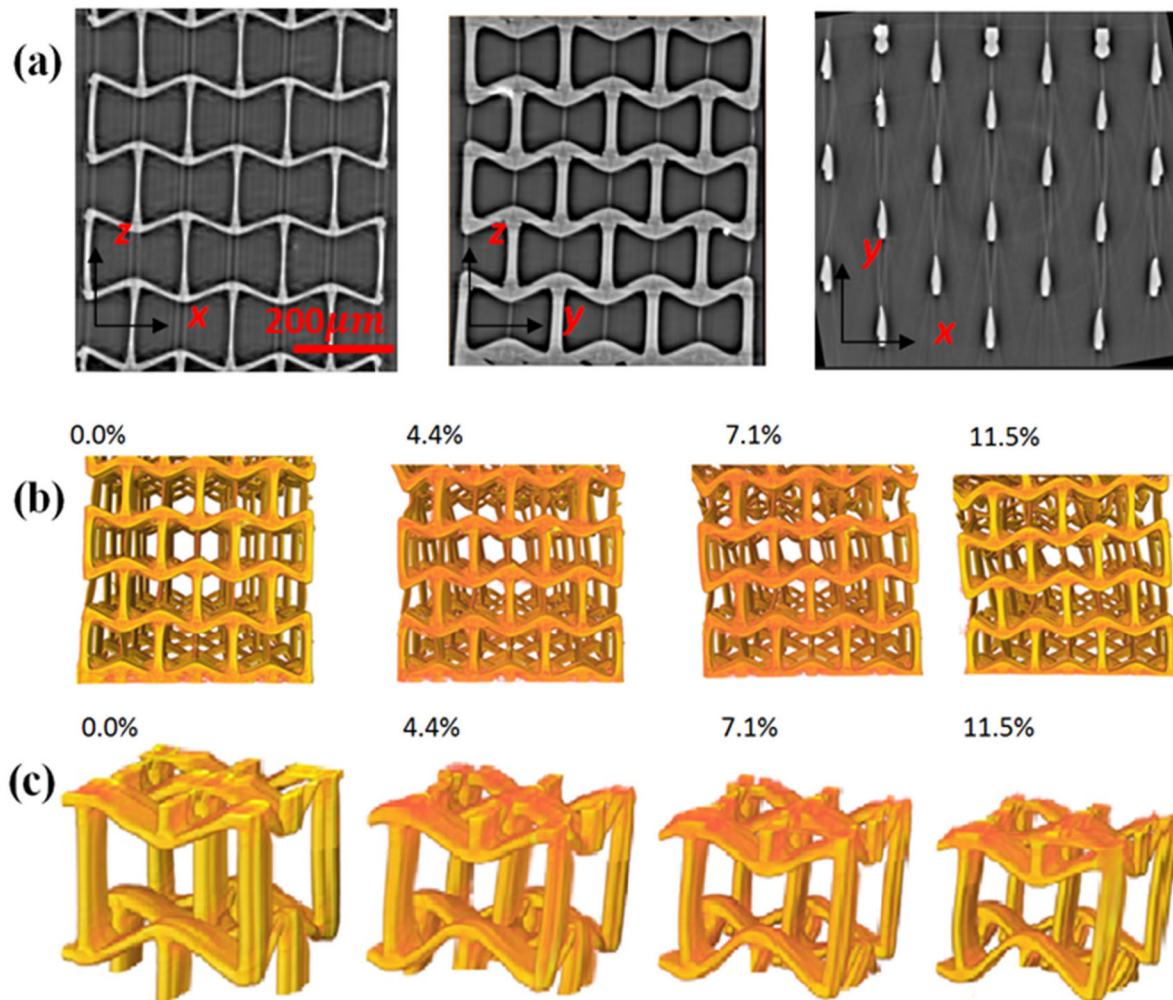


Fig. 4. Tomography images of as-fabricated 3D re-entrant lattice sample, global and local unit cell failure process of as-fabricated 3D re-entrant lattice (a), xz, yz and xy sliced cross-section views; (b), global deformation process of the sample at strain level: $\varepsilon_z=0.0\%$, 4.4% , 7.1% and 11.5% , respectively; (c), local deformation process of unit cell in the middle of the 3D re-entrant sample at strain level: $\varepsilon_z=0.0\%$, 4.4% , 7.1% and 11.5% , respectively.

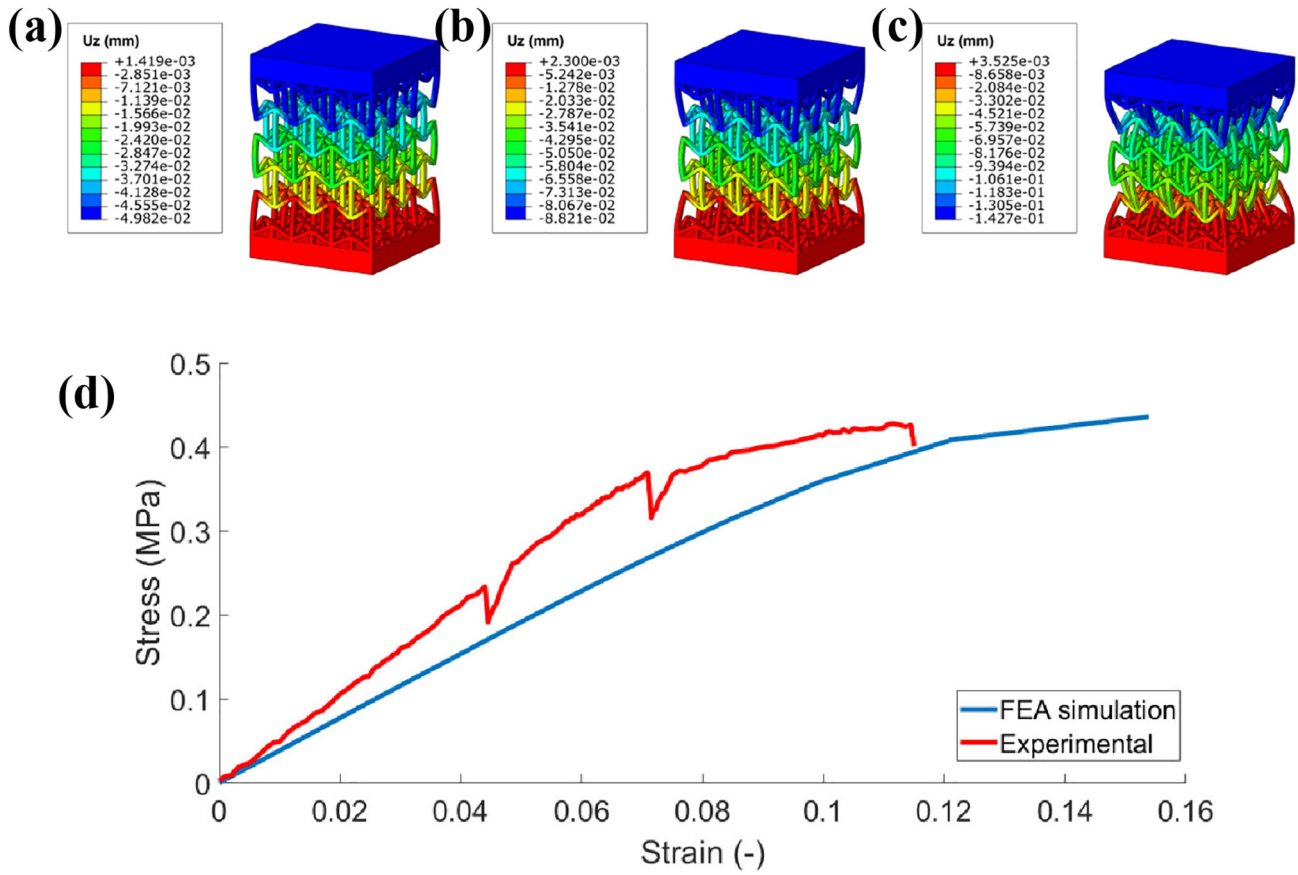


Fig. 5. Finite element modeling and experimental comparisons: global deformation process of the sample at strain level: (a), $\epsilon_z = 4.4\%$; (b), 7.1% and (c), 11.5% , respectively; (d), comparison between experimental and FEA simulation results.

The reconstructed 3D tomography images of the 3D re-entrant lattice based on SR- μ CT 3D imaging technique are shown in Fig. 6(a), where several typical types of defects were identified, such as: bulges, grooves, and stacks. Moreover, the 3D re-entrant lattice structure's self-weight will generate thickening effects along the building direction (along y axes) as a result of viscous fluid solidification during the P μ LSE additive manufacturing process. Fig. 6(b) shows the reconstructed 3D tomography images of 3D re-entrant unit cell. Fig. 6(c) illustrates the side views of a vertical strut with elevated dimensions and asymmetrical arc shapes on the upper and lower side surfaces along the building directions. Fig. 6(d) shows the fitted surface morphology of the vertical strut cross section. Similarly, Fig. 6(e) illustrates the side views of a diagonal strut with elevated dimensions and asymmetrical arc shapes on the upper and lower side surfaces along the building directions. Fig. 6(f) shows the fitted surface morphology of the diagonal strut cross section.

Afterwards, moment of inertia of different struts in 3D re-entrant lattices are analyzed, and comparisons between designed model and as-fabricated model reconstructed from tomography images are performed. The moments of inertia related to x and y principal axes of vertical and diagonal struts in the design 3D re-entrant lattices are: I_{Dx} and I_{Dy} , respectively. The moments of inertia related to x and y principal axes of vertical and diagonal struts in the as-fabricated 3D re-entrant lattices reconstructed from 3D tomography images are: I_{Bx} and I_{By} , respectively. In the moments of inertia analysis, geometrical dimensions variations of the 5 pieces of as-fabricated 3D re-entrant lattice structures are analyzed. In total, 30 slices are selected for each strut, where the moment of inertia of the as-fabricated strut are harvested and compared with the designed strut accordingly, and 50 vertical and diagonal struts are analyzed and averaged totally, where 10 diagonal and 10 vertical struts

are selected from each as-fabricated 3D re-entrant lattice sample. As shown in Table 3, the moments of inertia I_{By} for struts are always much bigger than I_{Dy} of the designed models for both vertical and diagonal struts, respectively, while the momentums of inertia I_{Bx} for struts are always smaller than I_{By} of the designed models for both vertical and diagonal struts, respectively.

Afterwards, geometrical dimensions variations of the 5 pieces of as-fabricated 3D re-entrant lattice structures are analyzed, 1000 slices from 50 diagonal struts, and 1000 slices from 50 vertical struts are selected for statistical analysis of the probability density of geometric defects, where 10 diagonal and 10 vertical struts are selected from each as-fabricated 3D re-entrant lattice sample, respectively. The average value \bar{u} and standard deviation σ of the horizontal and diagonal struts cross section side lengths are calculated separately. The superscripts "V" and "D" indicate the vertical and diagonal struts, respectively. Fig. 7 shows the strut cross section side length variation statistical results of the horizontal and diagonal struts, respectively.

5. Conclusions

In this paper, in situ micro-compression synchrotron X-Ray tomography 3D imaging device is designed and fabricated, and 3D micro re-entrant lattice mechanical metamaterials sample is fabricated with P μ LSE (Projection Micro Litho Stereo Exposure) 3D printing technology. Afterwards, in situ micro-compression X-Ray tomography 3D imaging of 3D micro re-entrant samples are performed for studying the deformation process, and comparisons between experiments and finite element analysis are performed for comparison, it is found that the as-fabricated struts are remarkably elongated along the building direction (y direction) during P μ LSE 3D printing process, resulting in elevated

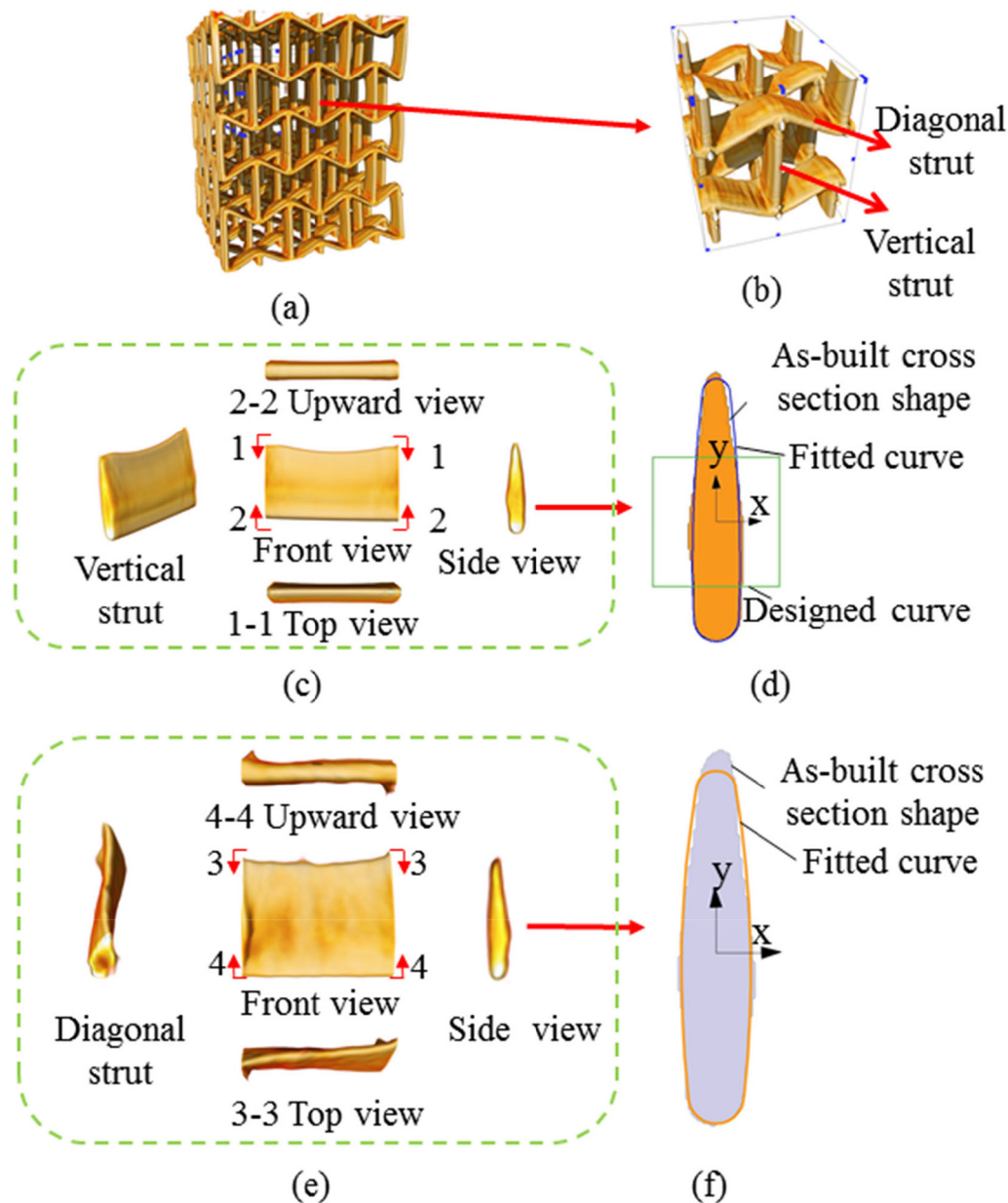


Fig. 6. Manufacture process induced geometrical defects of vertical and diagonal struts: (a) Reconstructed 3D re-entrant lattice strut and (b) unit cell; (c) spatial views of vertical strut; (d), fitted vertical strut morphology; (e) spatial views of diagonal strut; (f), fitted diagonal strut morphology.

experimental measured force during compression loading process, thus effects of manufacturing effects cannot be ignored and should be included into finite element models in the future for reliable mechanical behaviors prediction. It is the first time that such synchrotron X-Ray 3D tomography imaging experiment is performed for PµLSE 3D printed lattice mechanical metamaterials. The designed device is robust for studying the 3D deformation process and failure mechanisms of advanced materials and structures under X-Ray synchrotron tomography environment.

Table 3

The moment of inertia ratio of designed and tomography image reconstructed struts along different directions.

Ratio between designed and as-fabricated vertical strut		Ratio between designed and as-fabricated diagonal strut	
I_{Dx}/I_{Bx}	I_{Dy}/I_{By}	I_{Dx}/I_{Bx}	I_{Dy}/I_{By}
0.28 ± 0.025	5.91 ± 0.52	0.37 ± 0.024	10.62 ± 0.85

CRediT authorship contribution statement

Wenwang Wu: Data curation, Project administration, Funding acquisition. **Dexing Qi:** Writing - original draft. **Wenxia Hu:** Resources, Software, Validation. **Li Xi:** Funding acquisition, Investigation, Methodology, Project administration. **Lijuan Sun:** Formal analysis, Conceptualization. **Binbin Liao:** Formal analysis, Conceptualization. **Filippo Berto:** Writing - review & editing. **Guian Qian:** Writing - review & editing. **Dengbao Xiao:** Supervision, Writing - review & editing.

Acknowledgements

This research is supported by the National Natural Science Foundation of China (Grant 11702023; No. 11802031; No. 11972081). Beijing Municipal Science and Technology Commission (Z181100004118002). The authors would like to thank the BMF Precision Technology Co, Ltd. for supporting the micro/nano-scale 3D printing work.

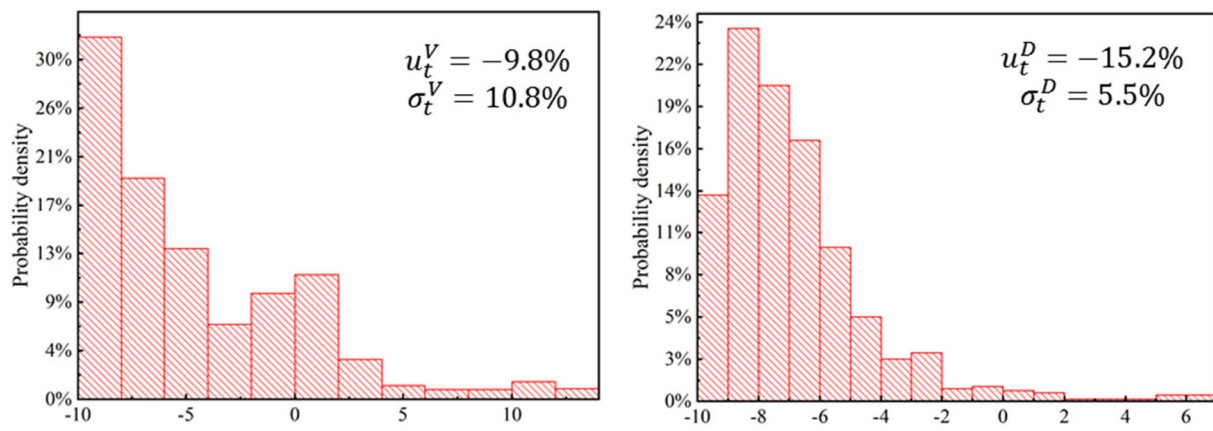


Fig. 7. Deviation of cross-section side length (a), vertical strut; (b), diagonal strut.

Declaration of competing interest

The authors declare NO conflict of interests.

References

- [1] W. Wu, Y. Tao, Y. Xia, J. Chen, H. Lei, L. Sun, D. Fang, Mechanical properties of hierarchical anti-tetrachiral metastructures, *Extreme Mech. Lett.* 16 (2017) 18–32.
- [2] R. Xia, X. Song, L. Sun, W. Wu, C. Li, T. Cheng, G. Qian, Mechanical properties of 3D isotropic anti-tetrachiral metastructure, *Physica Status Solidi (B) Basic Research* 255 (4) (2018), 1700343.
- [3] W. Wu, X. Song, J. Liang, R. Xia, G. Qian, D. Fang, Mechanical properties of anti-tetrachiral auxetic stents, *Comp. Struct.* 185 (2018) 381–392.
- [4] W. Wu, L. Geng, Y. Niu, D. Qi, X. Cui, D. Fang, Compression twist deformation of novel tetrachiral architected cylindrical tube inspired by towel gourd tendrils, *Extreme Mech. Lett.* 20 (2018) 104–111.
- [5] H. Yu, W. Wu, J. Zhang, J. Chen, H. Liao, D. Fang, Drastic tailorable thermal expansion chiral planar and cylindrical shell structures explored with finite element simulation, *Comp. Struct.* 210 (2019) 327–338.
- [6] W. Wu, D. Qi, H. Liao, G. Qian, L. Geng, Y. Niu, J. Liang, Deformation mechanism of innovative 3D chiral metamaterials, *Sci. Rep.* 8 (1) (2018) 12575.
- [7] X.L. Ruan, J.J. Li, X.K. Song, H.J. Zhou, W.X. Yuan, W.W. Wu, R. Xia, Mechanical Design of Antichiral-Reentrant Hybrid Intravascular Stent, *Int. J. Appl. Mech.* 10 (10) (2018) 1850105.
- [8] C. Ma, H. Lei, J. Liang, W. Wu, T. Wang, D. Fang, Macroscopic mechanical response of chiral-type cylindrical metastructures under axial compression loading, *Mater. Design* 158 (2018) 198–212.
- [9] Q. Lu, D. Qi, Y. Li, D. Xiao, W. Wu, Impact energy absorption performances of ordinary and hierarchical chiral structures, *Thin-Walled Struct.* 140 (2019) 495–505.
- [10] Y. Niu, J. Ge, J. Liang, H. Liao, W. Wu, Effects of disordered circular nodes dispersion and missing ligaments on the mechanical properties of chiral structures, *Physica Status Solidi (B) Basic Research* 256 (10) (2019), 1800586.
- [11] D. Xiao, X. Chen, Y. Li, W. Wu, D. Fang, The structure response of sandwich beams with metallic auxetic honeycomb cores under localized impulsive loading-experiments and finite element analysis, *Mater. Design* 176 (2019) 107840.
- [12] S. Duan, W. Wen, D. Fang, A predictive micropolar continuum model for a novel three-dimensional chiral lattice with size effect and tension-twist coupling behavior, *J. Mech. Phys. Solids* 121 (2018) 23–46.
- [13] R. Lakes, Foam structures with a negative Poisson's ratio, *Science* 235 (1987) 1038–1040.
- [14] D. Prall, R.S. Lakes, Properties of a chiral honeycomb with a Poisson's ratio of -1 , *Int. J. Mech. Sci.* 39 (1997) 305–307.
- [15] K. Bertoldi, P.M. Reis, S. Willshaw, T. Mullin, Negative Poisson's ratio behavior induced by an elastic instability, *Adv. Mater.* 22 (2010) 361–366.
- [16] H. Li, Y. Ma, W. Wen, W. Wu, H. Lei, D. Fang, In plane mechanical properties of Tetrachiral and Antitetrachiral hybrid Metastructures, *J. Appl. Mech.* 84 (2017), 081006.
- [17] N. Novak, M. Vesenjak, Z. Ren, Auxetic cellular materials—a review, *Stroj Vestn. J. Mech. Eng.* 62 (2016) 485–493.
- [18] X. Ren, R. Das, P. Tran, T.D. Ngo, Y.M. Xie, Auxetic metamaterials and structures: a review, *Smart Mater. Struct.* 27 (2018), 023001.
- [19] D. Qi, H. Yu, W. Hu, C. He, W. Wu, Y. Ma, Bandgap and wave attenuation mechanisms of innovative reentrant and anti-chiral hybrid auxetic metastructure, *Extreme Mech. Lett.* 28 (2019) 58–68.
- [20] Y. Han, W. Lu, Evolutionary design of nonuniform cellular structures with optimized Poisson's ratio distribution, *Mater. Design* 141 (2018) 384–394.
- [21] L.L. Hu, Z.R. Luo, Q.Y. Yin, Negative Poisson's ratio effect of re-entrant anti-trichiral honeycombs under large deformation, *Thin-Walled Struct.* 141 (2019) 283–292.
- [22] L. Ai, X.L. Gao, An analytical model for star-shaped re-entrant lattice structures with the orthotropic symmetry and negative Poisson's ratios, *Int. J. Mech. Sci.* 145 (2018) 158–170.
- [23] D. Xiao, Z. Dong, Y. Li, W. Wu, D. Fang, Compression behavior of the graded metallic auxetic reentrant honeycomb: experiment and finite element analysis, *Mater. Sci. Eng. A* 758 (2019) 163–171.
- [24] L. Geng, W. Wu, L. Sun, D. Fang, Damage characterizations and simulation of selective laser melting fabricated 3D re-entrant lattices based on in situ CT testing and geometric reconstruction, *Int. J. Mech. Sci.* 157–158 (2019) 231–242.
- [25] T. Wang, L. Wang, Z. Ma, G.M. Hulbert, Elastic analysis of auxetic cellular structure consisting of re-entrant hexagonal cells using a strain-based expansion homogenization method, *Mater. Design* 160 (2018) 284–293.
- [26] M.H. Fu, O.T. Xu, L.L. Hu, T.X. Yu, Nonlinear shear modulus of re-entrant hexagonal honeycombs under large deformation, *Int. J. Solid Struct.* 80 (2016) 284–296.
- [27] H. Wang, Z. Lu, Z. Yang, X. Li, A novel re-entrant auxetic honeycomb with enhanced in-plane impact resistance, *Comp. Struct.* 208 (2019) 758–770.
- [28] X.T. Wang, B. Wang, X.W. Li, L. Ma, Mechanical properties of 3D re-entrant auxetic cellular structures, *Int. J. Mech. Sci.* 131–132 (2017) 396–407.
- [29] Z.C. Eckel, C. Zhou, J.H. Martin, A.J. Jacobsen, W.B. Carter, T.A. Schaedler, Additive manufacturing of polymer-derived ceramics, *Science* 351 (2016) 58–62.
- [30] A. Vyatskikh, S. Delalande, A. Kudo, X. Zhang, C.M. Portela, J.R. Greer, Additive manufacturing of 3D nano-architected metals, *Nat. Commun.* 9 (2018) 593.
- [31] L. Brigo, J.E.M. Schmidt, A. Gandin, N. Michieli, P. Colombo, G. Brusatin, Multiscale ceramic components from preceramic polymers by hybridization of vat polymerization-based technologies, *Adv. Sci.* 5 (2018).
- [32] J.T. Muth, P.G. Dixon, L. Woish, L.J. Gibson, J.A. Lewis, Architected cellular ceramics with tailored stiffness via direct foam writing, *PNAS* 114 (2017) 1832–1837.
- [33] R.M. Latture, M.R. Begley, F.W. Zok, Defect sensitivity of truss strength, *J. Mech. Phys. Solids* 124 (2019) 489–504.
- [34] B. Lozanovski, M. Leary, P. Tran, D. Shidid, M. Qian, P. Choong, M. Brandt, Computational modelling of strut defects in SLM manufactured lattice structures, *Mater. Design* 171 (2019) 107671.
- [35] S. Guessasma, L. Tao, S. Belhabib, J. Zhu, W. Zhang, H. Nouri, Analysis of microstructure and mechanical performance of polymeric cellular structures designed using stereolithography, *Eur. Polym. J.* 98 (2018) 72–82.
- [36] Y. Amani, S. Dancette, P. Delroisse, A. Simar, E. Maire, Compression behavior of lattice structures produced by selective laser melting: X-ray tomography based experimental and finite element approaches, *Acta Mater.* 159 (2018) 395–407.
- [37] L. Liu, P. Kamm, F. García-Moreno, J. Banhart, D. Pasini, Elastic and failure response of imperfect three-dimensional metallic lattices: the role of geometric defects induced by selective laser melting, *J. Mech. Phys. Solids* 107 (2017) 160–184.
- [38] H.D. Carlton, J. Lind, M.C. Messner, N.A. Volkoff-Shoemaker, H.S. Barnard, N.R. Barton, M. Kumar, Mapping local deformation behavior in single cell metal lattice structures, *Acta Mater.* 129 (2017) 239–250.
- [39] Y. Sugimura, Mechanical response of single-layer tetrahedral trusses under shear loading, *Mech. Mater.* 36 (2004) 715–721.
- [40] T.B. Sercombe, X. Xu, V.J. Challis, R. Green, S. Yue, Z. Zhang, P.D. Lee, Failure modes in high strength and stiffness to weight scaffolds produced by selective laser melting, *Mater. Design* 67 (2015) 501–508.